Synthesis and characterization of WO_3, CuO and WO_3-CuO mixed nanomaterials oxide by using Sol-Gel Technique

Shubham Suresh Butle,
Department of Physics, Vidya Bharati Mahavidyalaya, Camp, Amravati,
Sant Gadge Baba Amravati University, Amravati, Maharashtra, India.

ABSTRACT: WO_3, CuO, and WO_3–CuO composite nanomaterials were successfully synthesized by the sol-gel method and systematically analyzed to investigate the effect of compositional variation on their structural and morphological properties. X-ray diffraction (XRD) confirmed the formation of phase-pure monoclinic CuO and nanocrystalline WO_3, while composite samples exhibited well-defined dual-phase diffraction patterns without secondary or impurity phases. Notably, increasing the WO_3 content led to a reduction in CuO crystallite size and total crystallinity, whereas CuO-rich compositions maintained sharper peaks, indicating enhanced crystalline order. Scanning electron microscopy (SEM) revealed pronounced morphological evolution: CuO-rich samples displayed highly porous, granular surfaces, whereas increasing WO_3 content produced denser, uniformly distributed nanostructures. The combination of XRD and SEM analyses highlights the tunable structural interactions in WO_3–CuO composites. The novelty of this work lies in the controlled modulation of crystallite size, porosity, and microstructure via compositional tuning, enabling optimization of these nanomaterials for advanced functional applications including gas sensing, catalysis, photocatalysis, and energy storage.

Keywords: WO_3; CuO; Metal oxide composites; sol-gel method;

1. Introduction

Nanomaterials have emerged as one of the most significant classes of advanced materials due to their unique physicochemical properties, which arise from their nanoscale dimensions and high surface-to-volume ratios. These attributes make them highly valuable for applications in catalysis, energy storage, sensing, optoelectronics, and environmental monitoring. Among various nanomaterials, metal-oxide semiconductors such as tungsten oxide (WO_3) and copper oxide (CuO) have attracted considerable attention. WO_3, an n-type semiconductor, is widely recognized for its excellent chemical stability, high sensitivity toward oxidizing gases, and strong electrochromic and catalytic behavior [1-2]. CuO, a p-type semiconductor, is known for its low toxicity, cost-effectiveness, and remarkable activity in chemical sensing and catalysis. When combined to form WO_3–CuO hybrid nanocomposites, these materials often exhibit enhanced gas-sensing performance due to synergistic effects arising from the formation of p-n heterojunctions, increased surface reactivity, and improved charge-transfer processes.

The synthesis of metal-oxide nanomaterials using the sol-gel method offers notable advantages, including simplicity, low processing temperature, cost-effectiveness, and excellent control over particle size and composition. This technique enables the formation of uniform, highly porous nanostructures that are favorable for gas-sensing applications. Structural characterization of the synthesized materials is commonly performed using X-ray diffraction (XRD), which provides insights into phase formation, crystallinity, and lattice structure. Meanwhile, scanning electron microscopy (SEM) allows detailed observation of surface morphology, particle size, and nanostructural features, which play critical roles in determining sensor performance. Gas-sensing studies further evaluate the response, sensitivity, selectivity, and response–recovery behaviors of the nanomaterials toward target gases.

In this study, WO_3, CuO, and their hybrid nanocomposites (NC-1, NC-2, and NC-3) with varying stoichiometric ratios were synthesized via the sol–gel method and systematically characterized using XRD and SEM to assess their structural and morphological properties [3-4].

1.1 Tungsten Oxide (WO_3)

Tungsten oxide (WO_3) nanoparticles are widely studied n-type semiconductor materials known for their excellent chemical stability, wide band gap (2.6–3.0 eV), and strong redox activity. At the nanoscale, WO_3 exhibits a significantly enhanced surface-to-volume ratio, increased surface reactivity, and tunable electronic properties, all of which make it highly suitable for advanced sensing technologies. WO_3 nanoparticles possess multiple crystalline phasessuch as monoclinic, hexagonal, and orthorhombiceach contributing uniquely to their optical, catalytic, and electrical behavior. In gas-sensing applications, WO_3 is especially valued for its high sensitivity toward oxidizing gases such as NO_2, O_2, CO_2 and H_2O_2, as well as certain reducing gases including H_2 and CO. Its sensing mechanism primarily involves changes in electrical resistance caused by the adsorption and reaction of gas molecules on the nanoparticle surface, making surface morphology, porosity, and crystallinity critical factors in determining performance. Furthermore, WO_3 nanoparticles offer advantages such

as fast response and recovery times, good repeatability, thermal stability, and compatibility with various composite structures. These attributes position WO_3 as a promising material for next-generation gas sensors, environmental monitoring systems, and related nano-enabled detection technologies.

1.2 Copper Oxide (CuO)

Copper oxide (CuO) nanoparticles are p-type semiconductor materials with a narrow band gap of approximately 1.2–1.9 eV, making them highly responsive to changes in their surrounding chemical environment. Due to their low cost, non-toxicity, ease of synthesis, and strong catalytic activity, CuO nanoparticles have gained significant attention in applications such as gas sensors, catalysts, batteries, and antimicrobial coatings. At the nanoscale, CuO exhibits enhanced surface area, high defect density, and increased active sites, which greatly improve its interaction with gas molecules. In gas-sensing applications, CuO is particularly sensitive to reducing gases such as H_2, CO, NH_3, CO_2 and H_2S, where gas adsorption induces notable changes in electrical conductivity. Its sensing mechanism is governed by surface adsorption-desorption processes and hole-based charge transport, allowing CuO to deliver high sensitivity, good selectivity, and stable operating performance. Additionally, CuO's ability to form efficient p-n heterojunctions with n-type metal oxides further enhances its sensing efficiency, response speed, and detection limits. These characteristics make CuO nanoparticles a highly promising material for developing advanced gas-sensing devices and environmental monitoring technologies [5].

2. Sol-Gel technique for nanomaterials materials synthesis

The sol-gel technique is a widely used chemical synthesis method for producing high-purity, homogeneous nanomaterials with precise control over composition and microstructure. In this process, metal alkoxides or inorganic salts undergo hydrolysis and condensation reactions to form a colloidal suspension (sol), which gradually evolves into a three-dimensional gel network. The resulting gel can be dried and calcined to obtain nanostructured powders, thin films, or porous materials. The sol–gel method is highly valued for its simplicity, low processing temperature, cost-effectiveness, and ability to achieve uniform particle size distribution at the nanoscale [6]. It also enables the incorporation of multiple metal oxides, making it ideal for preparing composite or hybrid nanomaterials with tailored properties. Due to these advantages, the sol–gel technique is extensively used in the synthesis of nanomaterials for applications such as gas sensors, catalysts, coatings, optical devices, and electronic components.

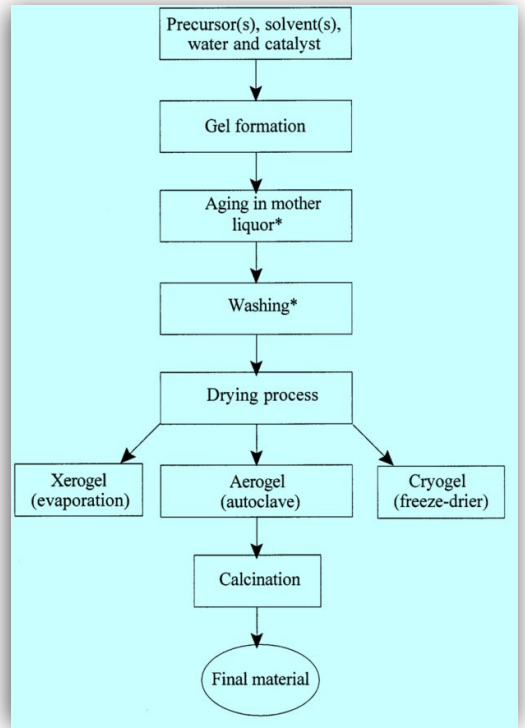

Fig. 1 Flow chart of sol-gel technique

3. Experimental Trial

Synthesis of WO_3, CuO Nanomaterials and WO_3–CuO Composites by the Sol–Gel Method

The synthesis of WO_3, CuO, and their composite WO_3–CuO nanomaterials was carried out using the sol–gel method at the UGC-recognized Research Center, Vidya Bharati Mahavidyalaya, Amravati, affiliated to Sant Gadge Baba Amravati University, Amravati. All the chemicals and raw materials required for the synthesis were readily available in the research laboratory, ensuring smooth and uninterrupted experimental work.

WO_3 and CuO nanomaterials were synthesized via a controlled sol-gel route using analytically pure metal precursors. Sodium tungstate dihydrate ($Na_2WO_4 \cdot 2H_2O$) was used as the tungsten source for WO_3, while copper nitrate trihydrate ($Cu(NO_3)_2 \cdot 3H_2O$) served as the copper precursor for CuO. Each precursor was dissolved separately in deionized water under continuous magnetic stirring to obtain clear and homogeneous solutions. Controlled hydrolysis and condensation reactions were initiated by adjusting the solution pH (typically maintained in the acidic range of pH 1–3 using dilute nitric), which promoted stable sol formation [7-8]. For the synthesis of individual oxides, the prepared sols were stirred for several hours and then aged at room temperature for 12-24h to ensure complete polymerization and network formation. Gelation occurred upon further aging, followed by drying of the gels at 80–100 °C for several hours to obtain xerogels. The dried xerogels were subsequently calcined in air at temperatures in the range of 400–600 °C for 2–4 h to remove organic residues and induce crystallization, yielding nanocrystalline WO_3 and highly crystalline CuO powders [7-8].

Fig. 2 Draining process of materials

WO_3–CuO composite nanomaterials were prepared by mixing the WO_3 and CuO sols in predetermined stoichiometric ratios of 20% WO_3–80% CuO (NC-1), 40% WO_3–60% CuO (NC-2), and 60% WO_3–40% CuO (NC-3). The mixed sols were vigorously stirred to achieve homogeneous molecular-level dispersion of both metal species. After aging, gelation, and drying under identical conditions as the individual sols, the composite xerogels were calcined under the same thermal treatment to obtain crystalline WO_3–CuO nanocomposites.

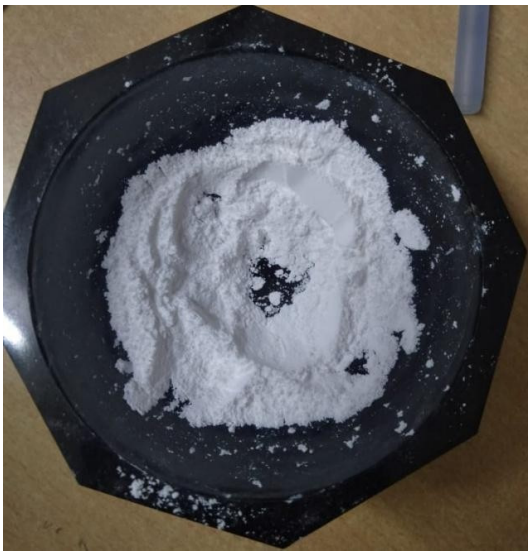

Fig. 3 Synthesized materials in powder form

The synthesized materials were further characterized using X-ray diffraction (XRD) to confirm their crystalline phases and structural purity, while scanning electron microscopy (SEM) was employed to study particle morphology, size distribution, and surface features. These nanomaterials and their composites were subsequently evaluated for their gas-sensing performance, demonstrating enhanced sensitivity and improved response behavior in hybrid WO_3-CuO systems [9-10].

4. Characterizations Tools

4.1 XRD Analysis

X-ray Diffraction (XRD) analysis is an essential technique used to determine the crystalline structure, phase composition, and purity of materials. It helps identify unknown compounds, detect impurities, and analyze structural properties such as lattice parameters, crystallite size, and internal strain. Because it is non-destructive, XRD allows researchers to study materials without altering them, making it highly valuable in fields like materials science, geology, chemistry, metallurgy, and pharmaceuticals. Overall, XRD provides crucial insights into the structural characteristics of materials, enabling better understanding, development, and quality control of various products and technologies.

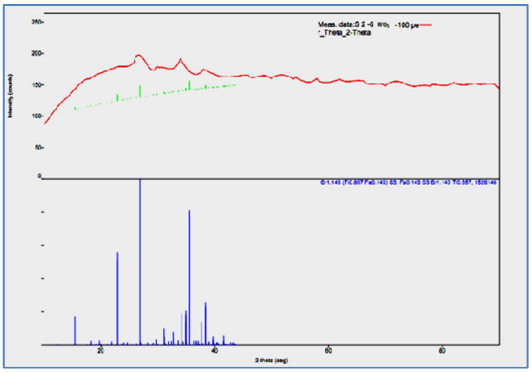

Fig. 4 XRD of WO_3

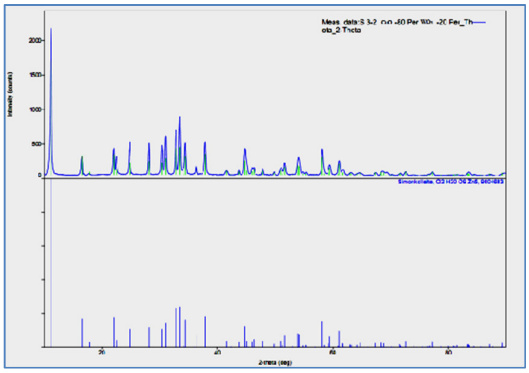

Fig. 5 XRD of 20%WO_3-80%CuO

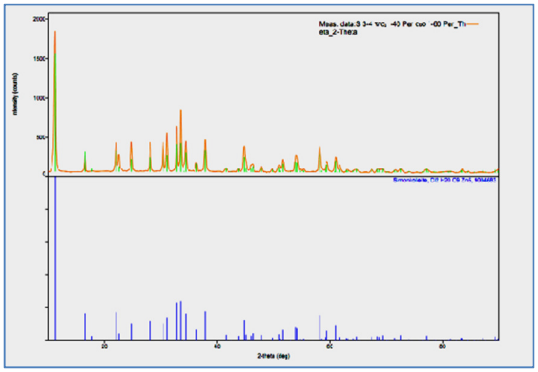

Fig. 6 XRD of 40%WO_3-60%CuO

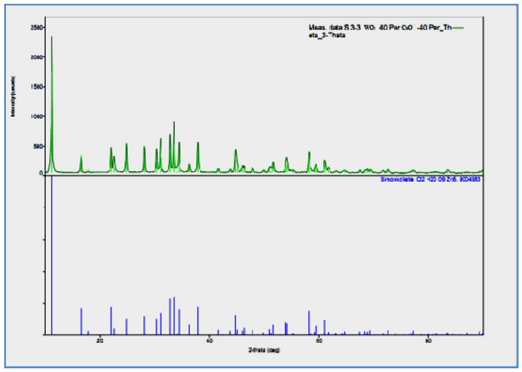

Fig. 7 XRD of 60%WO_3-40%CuO

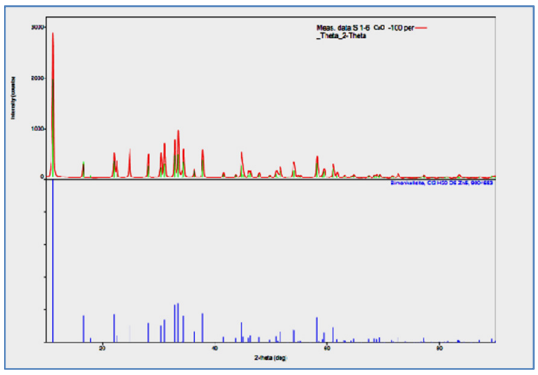

Fig. 8 XRD of CuO

Fig. 4 - XRD of WO_3

The X-ray diffraction (XRD) pattern of the synthesized WO_3 confirms the formation of phase-pure nanocrystalline monoclinic WO_3, with diffraction peaks matching well with standard JCPDS data. No impurity peaks are observed, indicating high structural purity. The diffraction peaks are noticeably broadened, revealing the nanocrystalline nature of the material. The average crystallite size, estimated using the Scherrer equation from the most intense peak (~26.6°), is found to be ~18–25 nm. The lattice parameters calculated for monoclinic WO_3 are approximately a ≈ 7.30 Å, b ≈ 7.54 Å, c ≈ 7.69 Å, with a monoclinic angle β ≈ 90.9°, which are in good agreement with reported values. Minor deviations are attributed to size-induced lattice strain [11-12].

Fig. 5 - XRD of 20% WO_3-80% CuO

The XRD pattern of the 20% WO_3–80% CuO composite confirms the presence of two distinct crystalline phases, monoclinic CuO (dominant) and monoclinic WO_3, with no impurity or secondary phases. The intense and sharp diffraction peaks mainly correspond to CuO, while the weaker peaks in the 23–27° range are attributed to WO_3, reflecting the CuO-rich composition. The absence of peak shifting indicates that both oxides retain their individual crystal structures in the composite. Quantitative analysis using the Scherrer equation reveals an average crystallite size of ~30–40 nm for CuO and ~18–25 nm for WO_3, confirming the nanocrystalline nature of the composite. The calculated lattice parameters closely match standard monoclinic values for CuO (a ≈ 4.68 Å, b ≈ 3.42 Å, c ≈ 5.13 Å, β ≈ 99.5°) and WO_3 (a ≈ 7.30 Å, b ≈ 7.54 Å, c ≈ 7.69 Å, β ≈ 90.9°). Minor variations are attributed to nanoscale size effects and interfacial strain.

Fig. 6 - XRD of 40% WO_3-60% CuO

The XRD pattern of the 40% WO_3–60% CuO composite confirms the coexistence of monoclinic WO_3 and monoclinic CuO without any secondary phases, indicating successful composite formation. Compared to CuO-rich samples, the WO_3 peak intensities in the 23–27° range are noticeably enhanced, reflecting the increased WO_3 content, while CuO remains the dominant phase. No peak shifting is observed, confirming that both oxides retain their individual crystal structures. Quantitative analysis using the Scherrer equation yields average crystallite sizes of ~28–35 nm for CuO and ~18–24 nm for WO_3, indicating nanocrystalline behavior. The calculated lattice parameters closely match standard monoclinic values for CuO (a ≈ 4.68 Å, b ≈ 3.42 Å, c ≈

5. 13 Å, β ≈ 99.5°) and WO_3 (a ≈ 7.30 Å, b ≈ 7.54 Å, c ≈ 7.69 Å, β ≈ 90.9°). Minor deviations are attributed to size-induced strain and interfacial effects.

Fig. 7 – XRD of 60% WO_3–40% CuO

The XRD pattern of the 60% WO_3–40% CuO composite confirms the coexistence of monoclinic WO_3 (dominant phase) and monoclinic CuO, with no secondary or impurity phases. The increased intensity of WO_3 peaks in the 23–27° region and the reduced CuO peak intensities reflect the WO_3-rich composition. The absence of peak shifting indicates that both oxides retain their individual crystal structures. Quantitative analysis using the Scherrer equation shows average crystallite sizes of ~15–22 nm for WO_3 and ~25–32 nm for CuO, confirming the nanocrystalline nature of the composite. The calculated lattice parameters are consistent with standard monoclinic values for WO_3 (a ≈ 7.30 Å, b ≈ 7.54 Å, c ≈ 7.69 Å, β ≈ 90.9°) and CuO (a ≈ 4.68 Å, b ≈ 3.42 Å, c ≈ 5.13 Å, β ≈ 99.5°), with minor deviations due to nanoscale strain.

Fig. 8 – XRD of CuO

The X-ray diffraction (XRD) pattern of the synthesized CuO clearly confirms the formation of phase-pure monoclinic CuO without the presence of any secondary or impurity phases. All observed diffraction peaks can be well indexed to standard monoclinic CuO reflections, indicating successful synthesis. The peaks are sharp and intense, revealing the high crystalline nature of the material. Quantitative crystallite size analysis was performed using the Scherrer equation, based on the most intense diffraction peak located at approximately 35.5°, yielding an average crystallite size in the range of 35–45 nm. This relatively large crystallite size is consistent with the narrow peak widths observed in the XRD pattern. The calculated lattice parameters (a ≈ 4.68 Å, b ≈ 3.42 Å, c ≈ 5.13 Å, β ≈ 99.5°) closely match the reported standard values for monoclinic CuO, confirming the structural stability and good crystallinity of the synthesized material [13-14].

Composition	**Dominant Phase**	**Crystallite Size, D (nm)**	**Micro-strain, ε ($\times10^{-3}$)**	**Dislocation Density, δ ($\times10^{14}$ m^{-2})**
WO_3	WO_3	18–25	2.8–3.5	1.6–3.1
20% WO_3–80% CuO	CuO	30–40 (CuO) 18–25 (WO_3)	1.6–2.2 (CuO) 2.8–3.4 (WO_3)	0.6–1.1 (CuO) 1.6–3.1 (WO_3)
40% WO_3–60% CuO	CuO	28–35 (CuO) 18–24 (WO_3)	1.8–2.5 (CuO) 2.9–3.6 (WO_3)	0.8–1.3 (CuO) 1.7–3.0 (WO_3)
60% WO_3–40% CuO	WO_3	15–22 (WO_3) 25–32 (CuO)	3.2–4.0 (WO_3) 2.0–2.6 (CuO)	2.1–4.4 (WO_3) 1.0–1.6 (CuO)
CuO	CuO	35–45	1.2–1.6	0.5–0.8

Table 1. XRD-Derived Structural Parameters of WO_3, CuO and WO_3–CuO Composites

4.2 SEM Analysis

Scanning Electron Microscopy (SEM) analysis is a powerful tool used to examine the surface morphology and microstructural features of materials with high resolution. It provides detailed images of surface topography, texture, and composition, allowing researchers to study particle size, shape, porosity, and surface defects. SEM is widely used in materials science, biology, nanotechnology, and electronics to understand material behavior, improve product design, and ensure quality control. Its ability to provide both qualitative and quantitative information makes SEM an indispensable technique for characterizing materials at the micro and nanoscale [15].

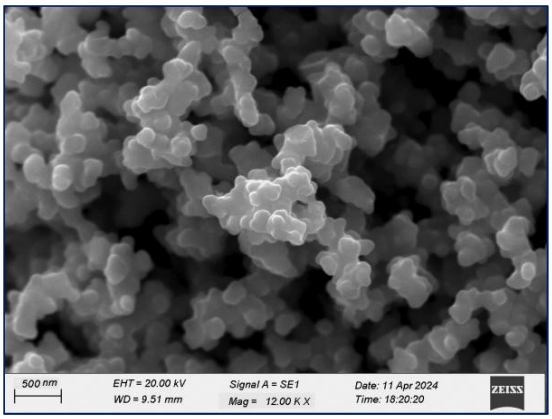

Fig. 9 SEM WO_3

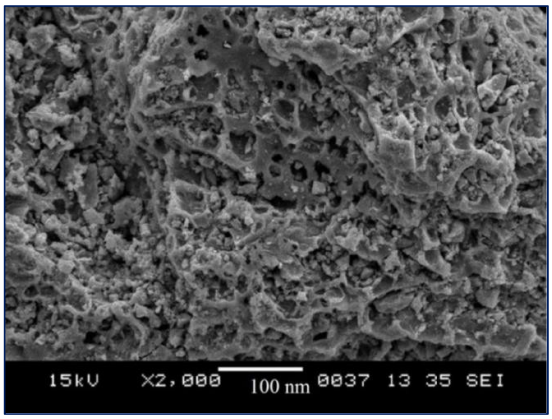

Fig. 10 SEM of 20%WO_3-80%CuO

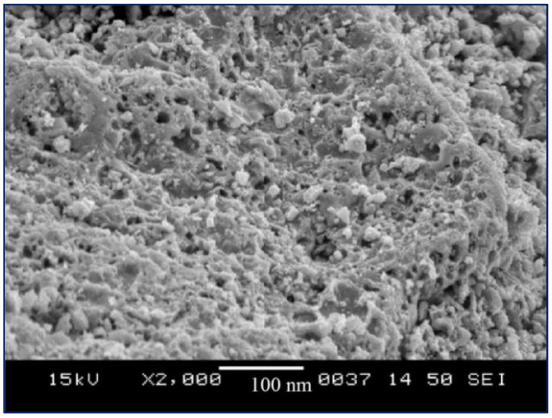

Fig. 11 SEM of 40%WO_3-60%CuO

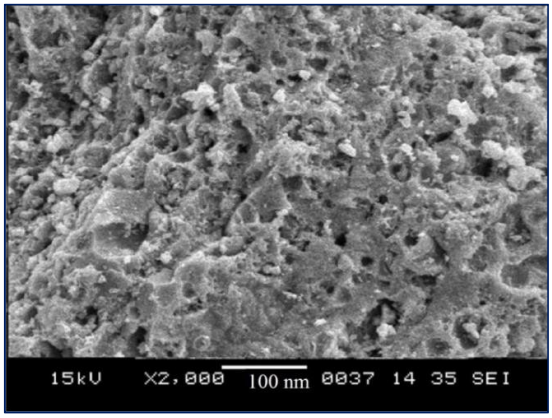

Fig. 12 SEM of 60%WO_3-40%CuO

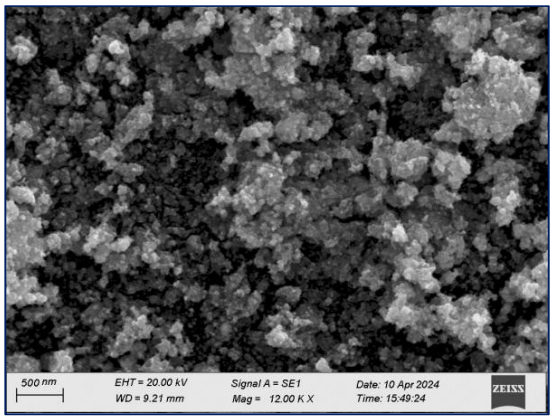

Fig. 13 SEM CuO

The SEM micrographs of WO_3, CuO, and their composites reveal distinct morphological features corresponding to the varying compositions and intrinsic structural characteristics of the two metal oxides. Pure WO_3 exhibits nanosized, nearly spherical grains with relatively uniform clustering and moderate agglomeration arising from high surface energy, resulting in a compact nano-agglomerated morphology. In contrast, pure CuO displays a rough, highly textured, granular surface with larger crystallites and pronounced porosity, characteristic of monoclinic CuO. This clear morphological contrast between the two pristine oxides governs the microstructural evolution observed in the composite samples.

A systematic correlation between SEM-observed morphology, bulk density, and total porosity is evident across all compositions. The total porosity (ϕ) was estimated using the standard pycnometric density method, which is widely validated in the literature for porous ceramics and metal-oxide materials. In this approach, porosity is calculated using the relation

$$\phi = 1 - \frac{\rho_{\text{bulk}}}{\rho_{\text{true}}}$$

where the bulk density (ρ_bulk) is obtained from the mass–volume ratio of the pellets and the true density (ρ_true) is determined by pycnometry. This method provides a reliable estimate of total porosity and is routinely employed for comparative analysis of porous oxide systems [16].

Pure CuO exhibits a highly porous morphology with interconnected voids, corresponding to a low bulk density of 2.30 g cm^{-3} and a high porosity of 64.2%. In contrast, pure WO_3 shows improved packing efficiency with a higher bulk density (3.40 g cm^{-3}) and lower porosity (52.7%), consistent with its compact nano-grain structure. The 20% WO_3–80% CuO composite remains CuO-dominated, displaying a flaky and open pore framework, with a bulk density of 2.52 g cm^{-3} and porosity of 61.6%. Increasing the WO_3 content to 40% leads to partial filling of CuO-induced voids by WO_3 nanoparticles, improving packing efficiency and reducing porosity to 59.3% (ρ_bulk = 2.74 g cm^{-3}), resulting in a more homogeneous microstructure.

The 60% WO_3–40% CuO composite exhibits a WO_3-dominated morphology characterized by a denser and more interconnected nano-grain network with significantly reduced large pores. Correspondingly, the bulk density increases to 2.96 g cm^{-3}, while the porosity decreases to 57.0%, confirming progressive densification

with increasing WO_3 content. Although the pycnometric method estimates only total porosity and does not distinguish between open and closed pores, the observed porosity trends are consistent with pore-structure evolution commonly reported from BET surface area analysis and mercury intrusion porosimetry in similar metal-oxide systems. Thus, the density-derived porosity values provide reliable support for the SEM-observed transition from highly porous CuO-rich morphologies to more compact WO_3-rich composites [17-18].

Sample	ρ_bulk (g cm^{-3})	ρ_true (g cm^{-3})	Porosity (%)
CuO	2.30	6.42	64.2
20% WO_3 – 80% CuO	2.52	6.57	61.6
40% WO_3 – 60% CuO	2.74	6.73	59.3
60% WO_3 – 40% CuO	2.96	6.88	57.0
WO_3	3.40	7.19	52.7

Table 2. Bulk density, true density, and estimated total porosity of WO_3–CuO samples

Combined XRD and SEM Correlation for WO_3, CuO, and Their Composites

The structural and microstructural characteristics of WO_3, CuO, and their composites were investigated using XRD and SEM, revealing a clear correlation between crystallinity, phase composition, and morphology. XRD patterns confirmed that pure WO_3 forms a phase-pure monoclinic structure with nanosized crystallites (~18–25 nm), while pure CuO exhibits phase-pure monoclinic CuO with relatively larger crystallites (~35–45 nm). Composites display the coexistence of monoclinic WO_3 and CuO phases without secondary impurities, with the dominant phase shifting from CuO-rich to WO_3-rich as the composition changes. Crystallite sizes calculated via the Scherrer equation indicate that WO_3 crystallites remain small across all composites (~15–25 nm), whereas CuO crystallite size decreases slightly in WO_3-rich compositions (~25–35 nm), suggesting nanoscale interfacial interactions.

SEM micrographs complement the XRD data by revealing morphological evolution corresponding to these crystallographic trends. Pure WO_3 exhibits compact, nearly spherical nanosized grains with moderate agglomeration, consistent with its smaller crystallite size and higher packing efficiency observed in XRD. In contrast, pure CuO shows rough, granular grains with pronounced porosity, in agreement with its larger crystallites. Composites demonstrate intermediate morphologies: 20% WO_3–80% CuO remains CuO-dominated with flaky, porous frameworks, while increasing WO_3 content to 40–60% progressively fills intergranular voids, producing denser, more interconnected nano-grain networks. Density-derived total porosity calculated using the pycnometric method decreases from 64.2% (pure CuO) to 57.0% (60% WO_3 composite), consistent with the observed densification in SEM images and the XRD-indicated crystallite refinement [19-20].

General, the combined XRD–SEM analysis reveals a strong structure–morphology correlation: smaller WO_3 crystallites promote better packing and reduced porosity, while CuO-rich phases favor open, highly porous morphologies. This interplay between crystallite size, phase distribution, and microstructure is critical for tailoring the physical properties and functional performance of WO_3–CuO composites, including their gas-sensing behavior.

Influence of Morphology on Functional Applications

The morphological features of WO_3, CuO, and their composites, as revealed by SEM and supported by XRD analysis, play a critical role in determining their functional performance in applications such as gas sensing, catalysis, and energy storage. Pure WO_3, with its compact, nearly spherical nanosized grains and moderate agglomeration, exhibits high surface area-to-volume ratios and uniform grain connectivity. This morphology ensures efficient electron transport and surface reactivity, making WO_3 particularly suitable for applications requiring fast charge transfer or selective gas adsorption.

In contrast, pure CuO displays rough, granular, and highly porous structures with larger crystallites. The interconnected voids enhance surface accessibility and adsorption capacity, which is advantageous for gas-sensing applications where high surface interaction is critical. However, the excessive porosity may reduce mechanical stability and limit electron percolation in devices requiring dense contacts [21].

In composite materials, the combination of WO_3 and CuO results in tunable morphologies that balance porosity, surface area, and grain connectivity. CuO-rich composites retain high porosity and open frameworks, promoting rapid gas diffusion and adsorption. Increasing WO_3 content progressively fills the intergranular voids, creating a denser and more interconnected nano-grain network. This densification improves mechanical stability and electron transport while maintaining sufficient active sites for functional reactions. As a result, the WO_3–CuO composites exhibit optimized morphology-dependent properties, such as enhanced gas-sensing sensitivity, faster response/recovery times, and improved catalytic activity, demonstrating the strong interplay between microstructure and functional performance [22].

5. Conclusions

In this work, WO_3, CuO, and their composite systems with varying ratios were successfully characterized using X-ray diffraction (XRD) and scanning electron microscopy (SEM). The XRD results confirmed the formation of distinct crystalline phases for each oxide: nanocrystalline WO_3 with broadened peaks and highly crystalline monoclinic CuO with sharp, intense diffraction lines. The composite samples consistently exhibited two-phase patterns without evidence of new compound formation, indicating that WO_3 and CuO coexist as separate crystalline phases. The relative intensities of the peaks reflected the compositional variations, with WO_3-rich composites showing stronger WO_3 peaks and CuO-rich composites demonstrating CuO-dominant crystallinity [23].

SEM analysis provided detailed insights into the surface morphology and particle interactions within the materials. Pure WO_3 displayed uniform nanosized particles with noticeable agglomeration, while pure CuO showed coarse, granular, and porous structures characteristic of larger crystallites. The composite samples demonstrated a clear morphological transition with increasing WO_3 content: CuO-rich composites retained a rough, porous texture, whereas WO_3-rich composites exhibited smoother, denser nano-grain structures. These morphological changes were consistent with the XRD results and revealed improved homogeneity and structural refinement with increasing WO_3 concentration. The complementary information obtained from XRD and SEM confirms that the microstructural and morphological properties of WO_3–CuO composites are highly tunable through composition [24].

Author contributions: The other author helped to finalize the finding and to modify the synthesize the materials.

Data availability: No datasets were generated or analysed during the current study.

Declarations

Competing interests: The authors declare no competing interests.

References

1. K. R. Park, H. B. Cho, J. Lee, Y. Song, W.-B. Kim, Y.-H. Choa, Design of highly porous SnO_2-CuO nanotubes for enhancing H_2S gas sensor performance, Sensor. Actuator. B Chem. 302 **(2020)** 127179, https://doi.org/10.1016/j.snb.2019.127179.

2. T.T.N. Hoa, D.T.T. Le, N. Van Toan, N. Van Duy, C.M. Hung, N. Van Hieu, N.D. Hoa, Highly selective H_2S gas sensor based onWO_3-coated SnO_2nanowires, Mater. Today Commun. 26 **(2021)** 102094, https://doi.org/10.1016/j.mtcomm.2021.102094.

3. Selvam, G. K. P., Amador, M. de la L. O., & Álvarez, A. M.. Gas sensing capabilities of sol–gel dip-coated pure SnO_2 thin films for CO and C_3H_8 detection. Journal of Materials Science: **(2024)** Materials in Electronics. https://doi.org/10.1007/s10854-024-13288-8

4. G. Jung, S. Hong, Y. Jeong, W. Shin, J.-W. Park, D.H. Kim, highly selective and low-power carbon monoxide gas sensor based on the chain reaction of oxygen and carbon monoxide to WO_3, ACS Appl. Mater. Interfaces **(2022),** https://doi.org/10.1021/acsami.1c25221.

5. H.U. Khan, M. Tariq, M. Shah, et al., Inquest of highly sensitive, selective and stable ammonia (NH_3) gas sensor: structural, morphological and gas sensing properties of polyvinylpyrrolidone (PVP)/CuO nanocomposite, Synth. Met. 268 **(2020)** 116482, https://doi.org/10.1016/j.synthmet.2020.116482.

6. S. Mei, F. Jiang, N. Liu, Z. Feng, Y. Zheng, W. Yang, N. Zhang, Sol-gel synthesis of magnesium oxide nanoparticles and their evaluation as a therapeutic agent for the treatment of osteoarthritis, Nanomedicine (**2024**) 1–12, https://doi.org/10.1080/17435889.2024.2382421.

7. Nagarjuna R, Challagulla S, Sahu P, Roy S, Reddy KR. Polymerizable sol–gel synthesis of nano-crystalline WO_3 and its photocatalytic Cr (VI) reduction under visible light. Adv. Powder Technol. (**2017**);28(12):3265–3273. https://doi.org/10.1016/j.apt.2017.09.030

8. Patel M, Mishra S, Verma R, Shikha D. Synthesis of ZnO and CuO nanoparticles via sol–gel method and its characterization by using various techniques. Discover Mater. (**2022**); 2:1. https://doi.org/10.1007/s43939-022-00022-6

9. Zhang X, Wang Z, Liu X, Zhao S, Li A. Synthesis of WO_3–CuO composite nanostructures and enhanced gas sensing properties toward NO_2 at low temperature. J. Mater. Sci. (**2021**); 56:7534–7548. https://doi.org/10.1007/s10853-021-05826-4

10. Kumar A, Singh S, Kim K-H, Deep A. WO_3–CuO heterostructured nanocomposites for high-performance NO_2 gas sensing: Synergistic effect of dual metal oxides. Sens. Actuators B Chem. (**2022**); 367:132038. https://doi.org/10.1016/j.snb.2022.132038

11. Altanany SM, El-Gammal OA, Badr YA, El-Adawy AA. Synthesis and characterization of CuO/WO_3 nanocomposite prepared by co-precipitation method: Structural and optical studies. AIP Conf. Proc. (**2018**); 2047:020014. https://doi.org/10.1063/1.5042381

12. Dursun S, Şen F, Öztürk Z, et al. Production of CuO–WO_3 hybrids and their dye removal capacity/performance from wastewater by adsorption/photocatalysis. J. Water Process Eng. (**2020**); 36:101390. https://doi.org/10.1016/j.jwpe.2020.101390

13. Patra N, Ravi G. Hydrothermal synthesis of CuO/WO_3 hybrid bifunctional composites with unprecedented dark adsorption and photocatalysis. Chem. Select. (**2024**); 9: e202400042. https://doi.org/10.1002/slct.202400042

14. Castaneda Mendoza M, Parra Vargas CA, Rincón Joya M, et al. Gas sensor properties of (CuO/WO_3)-$CuWO_4$ heterostructured nanocomposite materials. Materials (**2025**); 18(12):2896. https://doi.org/10.3390/ma18122896

15. Akhtar, K., Khan, S. A., Khan, S. B. & Asiri, A. M. Scanning Electron Microscopy: Principle and applications in nanomaterials characterization. In Scanning Electron Microscopy (**2018**). https://doi.org/10.1007/978-3-319-92955-2_4

16. Macedo RR, Ulsen C, Jacomo A, Figueiredo P, Nery G, Uliana D. Pycnometry for assessing porosity of fine recycled aggregates. Constr. Build. Mater. (**2021**); 298:125091. https://doi.org/10.1016/j.conbuildmat.2021.125091

17. Shimizu, Y., Hyodo, T., Egashira, M. & Yamazoe, N. Microstructure control of semiconductor gas sensors: effects of bulk density and porosity on sensing properties. Sens. Actuators B Chem. 77, 35–42 (**2001**). https://doi.org/10.1016/S0925-4005(01)00690-2

18. Hübner, M., Simion, C. E., Haensch, A., Barsan, N. & Weimar, U. CO sensing mechanism with CuO–WO_3 based gas sensors. Sens. Actuators B Chem. 151, 103–106 (**2010**). https://doi.org/10.1016/j.snb.2010.09.041

19. R. Molavi, M.H. Sheikhi, Facile wet chemical synthesis of Al-doped CuO nanoleaves for carbon monoxide gas sensor applications, Mater. Sci. Semicond. Process. 106 (**2020**) 104767, https://doi.org/10.1016/j.mssp.2019.104767.

20. Conde-Guevara, M., Tangirala, V.K.K., Méndez-Blas, A. et al. WO_3 film sensors: attributes in gas detection for CO_2. Journal of Materials Science: Materials in Electronics (**2025**). DOI: 10.1007/s 1085402515305

21. H. Jamalabadi, N. Alizadeh, Enhanced low-temperature response of PPy-WO_3 hybrid nanocomposite-based gas sensor deposited by electrospinning method for selective and sensitive acetone detection, IEEE Sensor. J. 17 (8) (**2017**) 2322–2328, https://doi.org/10.1109/jsen.2017.2662716.

22. Wang, Y., Zhang, S., Xiao, D., Wang, S., Zhang, T., Yang, X., & Heng, S.. CuO/WO_3 hollow microsphere p-n heterojunction sensor for continuous cycle detection of H_2S gas. Sensors and Actuators B: Chemical, (**2023**) Article No. 132823. https://doi.org/10.1016/j.snb.2022.132823

23. H. Ji, W. Zeng, Y. Xu, Y. Li, Nanosheet-assembled hierarchical WO_3 flower-like nanostructures: hydrothermal synthesis and NH_3-sensing properties, Mater. Lett. 250 (**2019**) 155–158, https://doi.org/10.1039/c8ra01818a.

24. Alaizeri, Z. M., Alhadlaq, H. A., Aldawood, S., Akhtar, M. J., & Ahamed, M. Bi_2O_3 -doped WO_3 nanoparticles decorated on rGO sheets: Simple synthesis, characterization, photocatalytic performance, and selective cytotoxicity toward human cancer cells (**2023**). ACS Omega. DOI https://doi.org/10.1021/acsomega.3c01644